11-24-2014

Configurational Thermodynamics of Alloyed Nanoparticles with Adsorbates

Lin-Lin Wang
Ames Laboratory, llw@ameslab.gov

Teck L. Tan
Agency for Science, Technology and REsearch

Duane D. Johnson
Iowa State University, ddj@iastate.edu

Configurational Thermodynamics of Alloyed Nanoparticles with Adsorbates

Abstract

Changes in the chemical configuration of alloyed nanoparticle (NP) catalysts induced by adsorbates under working conditions, such as reversal in core–shell preference, are crucial to understand and design NP functionality. We extend the cluster expansion method to predict the configurational thermodynamics of alloyed NPs with adsorbates based on density functional theory data. Exemplified with PdRh NPs having O-coverage up to a monolayer, we fully detail the core–shell behavior across the entire range of NP composition and O-coverage with quantitative agreement to in situ experimental data. Optimally fitted cluster interactions in the heterogeneous system are the key to enable quantitative Monte Carlo simulations and design.

Keywords

Materials Science and Engineering, Cluster expansion, First-principles, Nanoalloy, Pd, Rh, O, Core-shell nanoparticle

Comments

Reprinted with permission from Nano Lett. **2014**, 14(12), pp. 7077–7084, doi:10.1021/nl503519m.

NANO LETTERS

Letter

pubs.acs.org/NanoLett

Configurational Thermodynamics of Alloyed Nanoparticles with Adsorbates

Lin-Lin Wang,*[,†] Teck L. Tan,[‡] and Duane D. Johnson*[,†,§]

[†]Ames Laboratory, U.S. Department of Energy, Iowa State University, Ames, Iowa 50011, United States

[‡]Institute of High Performance Computing, Agency for Science, Technology and Research, Singapore 138632, Singapore

[§]Department of Materials Science and Engineering, Iowa State University, Ames, Iowa 50011, United States

Supporting Information

ABSTRACT: Changes in the chemical configuration of alloyed nanoparticle (NP) catalysts induced by adsorbates under working conditions, such as reversal in core−shell preference, are crucial to understand and design NP functionality. We extend the cluster expansion method to predict the configurational thermodynamics of alloyed NPs with adsorbates based on density functional theory data. Exemplified with PdRh NPs having O-coverage up to a monolayer, we fully detail the core−shell behavior across the entire range of NP composition and O-coverage with quantitative agreement to in situ experimental data. Optimally fitted cluster interactions in the heterogeneous system are the key to enable quantitative Monte Carlo simulations and design.

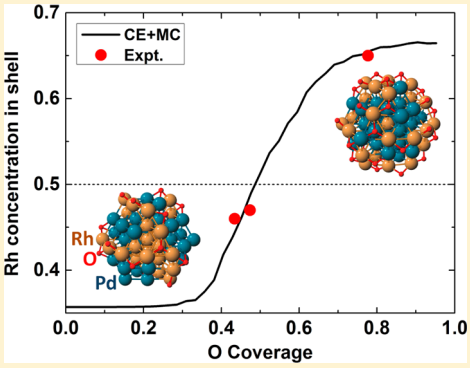

KEYWORDS: *Cluster expansion, first-principles, nanoalloy, Pd, Rh, O, core−shell nanoparticle*

For transition-metal alloyed nanoparticles (NPs) used as heterogeneous catalysts, besides the morphology[1−4] and structural[5−7] changes induced by the chemical environment in which they operate, a third type of change, alloy configuration or chemical order, can also be altered by adsorbates, such as their core−shell configurations.[8−11] Recently, in ambient pressure X-ray photoemission spectroscopy (AP-XPS) experiments, the $Pd_{0.5}Rh_{0.5}$ NP was observed[8−10] to switch back and forth between a Rh-rich shell in oxidizing conditions and a Pd-rich shell in reducing conditions. As many studies have shown, the enhanced catalytic functionality of nanoalloy catalysts highly depends on the configurational thermodynamics, or distribution of atoms on different sites.[12−15] Although certain core−shell configurations with different degree of mixing in alloyed NPs can be synthesized, the thermodynamic stability of such configurations is often an open question. Thus, an accurate description of the configurational thermodynamics of alloyed NPs, especially under chemical working conditions, is crucial to understand their functionality and stability for the design of new nanoalloy catalysts.

For alloyed NPs, the exponential number of alloy configurations with many different types of low-coordinated sites makes theoretical studies on configurational thermodynamic challenging. For example, a bare binary alloyed NP of 55 atoms without adsorbate has 2^{55} ($\sim 10^{16}$) possible alloy configurations. Monte Carlo[16] (MC) simulation to sample this configurational space requires millions of energy evaluation on-the-fly, not possible in a feasible time frame by density functional theory[17,18] (DFT) calculations alone. Here, by extending the cluster expansion[19] (CE) formalism of a nonexchangeable coupled lattice[20] to alloyed NPs with adsorbates, we treat substrate−adsorbate and adsorbate−adsorbate interactions on an equal footing to substrate−substrate interactions to study the thermodynamics in alloyed NPs and changes induced by adsorbates, including reversal of core−shell preference.

For adsorbate-induced changes in nanoalloy configurations, we study PdRh NPs.[21,22] These alloys are important for environmental and energy-saving technology, as part of the three-way catalysts in automobile converter.[23,24] PdRh NPs have been found to offer enhanced catalytic activity for CO oxidation,[10] NO reduction[25] and also Suzuki cross-coupling reaction[26] for organic molecule synthesis to bridge heterogeneous and homogeneous catalysis by varying size, shape, and composition. The improved catalytic properties have been attributed to many effects, such as new electronic states from alloying, Pd−Rh interfaces, and segregation behaviors induced by substrate and adsorbate. Among them, segregations induced by reaction condition were studied on thin films[27] and, more recently, on NPs to show a core−shell reversal[8,9] induced by adsorbates.

Here, to enable a quantitative description of the relation between core−shell behavior and O-coverage, we study the thermodynamics of O adsorption on a 55-atom cuboctahedral

Received: September 12, 2014
Revised: November 14, 2014
Published: November 20, 2014

core−shell NPs versus Rh composition and O-coverage (up to a monolayer) and compare with in situ AP-XPS data.[8,9] We find that only core−shell NPs with compositions near 50% Rh have the core−shell reversal induced by O-coverage due to NP geometric size effect, agreeing with observation.[9] The simulated shell concentration of Rh in the small $Pd_{0.5}Rh_{0.5}$ NP across the same effective O-coverage range also agrees with the experimental data on large NPs, reflecting the same origin from the relative strength of metal−O to metal−metal interactions.[8] Our study also reveals the detailed site occupations as functions of both the overall composition and O-coverage, providing design information for nanoalloy catalysts, especially the thermodynamically stable active sites under working conditions.

Computational Methods. The CE coupled with DFT calculations, proven enormously successful for bulk alloys,[28−37] has been recently extended to study the configurational thermodynamics of bare alloyed NPs without adsorbates,[38−43] such as to find the stable configurations of AgAu NPs[39] as multicore−shell and design PdPt NPs[40] for hydrogen evolution reaction. Notably, core−shell preferences of bare alloyed NPs without adsorbates exhibit a universal behavior that can be understood from impurity segregation energies[44] − determined by only cohesive energy (reflecting *d*-band filling) and atomic radius (reflecting *d*-bandwidth).

Within CE, any physical quantity as a function of configurational variables on fixed lattices can be expanded in the basis of a series of cluster correlation functions.[19] Here, for a system with two coupled lattices of nonexchangeable configurations, we expand the formation energy as

$$E(\sigma,\delta) = \sum_{\alpha\beta} V_{\alpha\beta}\Theta_{\alpha\beta}(\sigma,\delta) = \sum_{\alpha\beta} V_{\alpha\beta}\Phi_{\alpha}(\sigma)\Psi_{\beta}(\delta)$$
$$= V_0 + \Big(\sum_i V_i^{S}\sigma_i + \sum_{i,j} V_{ij}^{S}\sigma_i\sigma_j + \cdots\Big)$$
$$+ \Big(\sum_i V_i^{A}\delta_i + \sum_{i,j} V_{ij}^{A}\delta_i\delta_j + \cdots\Big) + \Big(\sum_{i,j} V_{ij}^{C}\sigma_i\delta_j + \cdots\Big) \quad (1)$$

where $\Theta_{\alpha\beta}(\sigma,\delta) = \Phi_{\alpha}(\sigma)\Psi_{\beta}(\delta)$ are the products of cluster correlation functions on two coupled lattices and $V_{\alpha\beta}$ are the corresponding effective cluster interactions (ECIs) to be determined via structural inversion and cluster selection.[45] Because the orthogonality of primitive basis functions is always preserved in the construction of high-dimensional vector space by outer (tensor) products, a coupled lattice with nonexchanging species that works for ionic systems[20] will also work for adsorbates on alloyed surfaces[46,47] and NPs. The second line is explicitly for a binary alloy substrate with one type of adsorbate, using site-occupation variables, σ_i or δ_i, equal 1 (0) if site i is occupied (not occupied). The ECIs for substrate, adsorbate and coupled clusters are denoted with superscript S, A, and C, respectively. As extended here, the CE enables coverage-dependent studies on the thermodynamics of alloyed NPs and surfaces with adsorbates.

The formation energy per site (E_f) for the PdRh NPs with O-coverage is defined as

$$E_f = \frac{1}{(N_S + N_A)}\Big[E_{tot} - n_{Rh}E_{Rh} - (N_S - n_{Rh})E_{Pd} - \frac{1}{2}n_O E_{O_2}\Big] \quad (2)$$

which is calculated from the DFT total energies of the adsorption system (E_{tot}) referenced to NPs of pure Pd (E_{Pd}) and Rh (E_{Rh}) as well as O_2 (E_{O_2}). The N_S, N_A, n_{Rh}, and n_O is the number of all the substrate, adsorbate sites, Rh, and O atoms, respectively. We should also define the overall Rh composition as $c_{Rh} = n_{Rh}/N_S$, the shell (core) concentration of Rh as $c_{Rh}^{shell} = n_{Rh}^{shell}/N_S^{shell}$ ($c_{Rh}^{core} = n_{Rh}^{core}/N_S^{core}$) and O-coverage as $\theta = n_O/N_S^{shell}$, where N_S^{shell} (N_S^{core}) is the number of shell (core) sites in the substrate.

Figure 1 shows the nonexchangeable coupled lattices to address O adsorption on a cuboctahedral alloyed PdRh NP (N_S = 55, N_A = 104, N_S^{shell} = 42 and N_S^{core} = 13). The O_h symmetry greatly reduces the number of symmetry unique types of site (or 1-body ECIs) required. As shown in Figure 1a, there are five and four types in the substrate and adsorbate lattices, respectively. An bridge-fcc (brf) site is on the edge of the NP, which can be viewed as bridge (brg) or fcc site from the perspective of {100} or {111} facet, respectively. The 4-fold hollow site on {100} facet is not included because its O binding strength is weaker than the neighboring brf site within a short distance and will experience destabilizing O−O repulsion, once the brf is occupied. Similarly, we exclude other O configurations and the corresponding clusters containing adsorbate sites having distances below $(1/2)\bar{a}$, half the averaged bulk lattice constant of Pd and Rh. This exclusion is appropriate because the shortest O−O distance in the full monolayer coverage is $(\sqrt{2}/2)\bar{a}$, and we are only interested in coverage up to 40 O, slightly less than the full monolayer. From a pool of 9 1-body, 96 2-body, and 403 3-body clusters, an optimally truncated CE is selected via a leave-one-out cross-validation (CV-1) score.

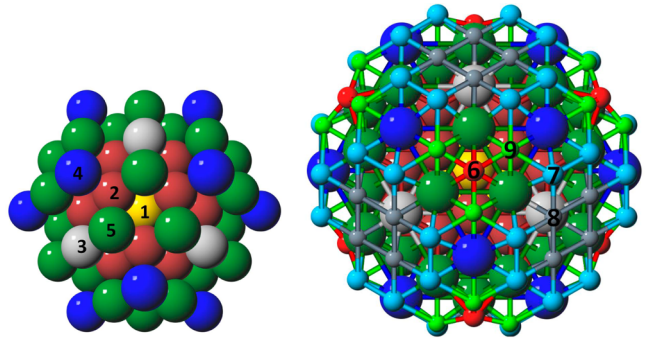

Figure 1. CE distinctive 1-body or symmetry inequivalent sites in the (a) substrate and (b) adsorbate sublattices of a 55-atom cuboctahedral NP with 104 adsorption sites. The substrate sites are composed of five types: 1 central-core, 12 s-core, 6 100-center, 12 corner, and 24 edge sites. The adsorbate lattice has four different types: 8 fcc, 48 brf, 24 brg, and 24 hcp sites. The sites are numbered and color-coded to show the nine inequivalent sites due to O_h symmetry: central-core (1), second-core (2), 100-center (3), corner (4), and edge (5) substrate site, along with fcc (6), brf (7), brg (8), and hcp (9) adsorption site.

We search for groundstates (GSs) and optimize CE simultaneously in an iterative approach by thermal annealing with MC simulation and DFT verification round-by-round. For the CE in such a heterogeneous system, we develop a new strategy to fit the ECIs via a two-step approach that accounts for the relative strength of the interactions, yielding CE sets with small prediction errors and fast convergence to the GSs. The specifics of fitting heterogeneous sets of ECIs for NP with

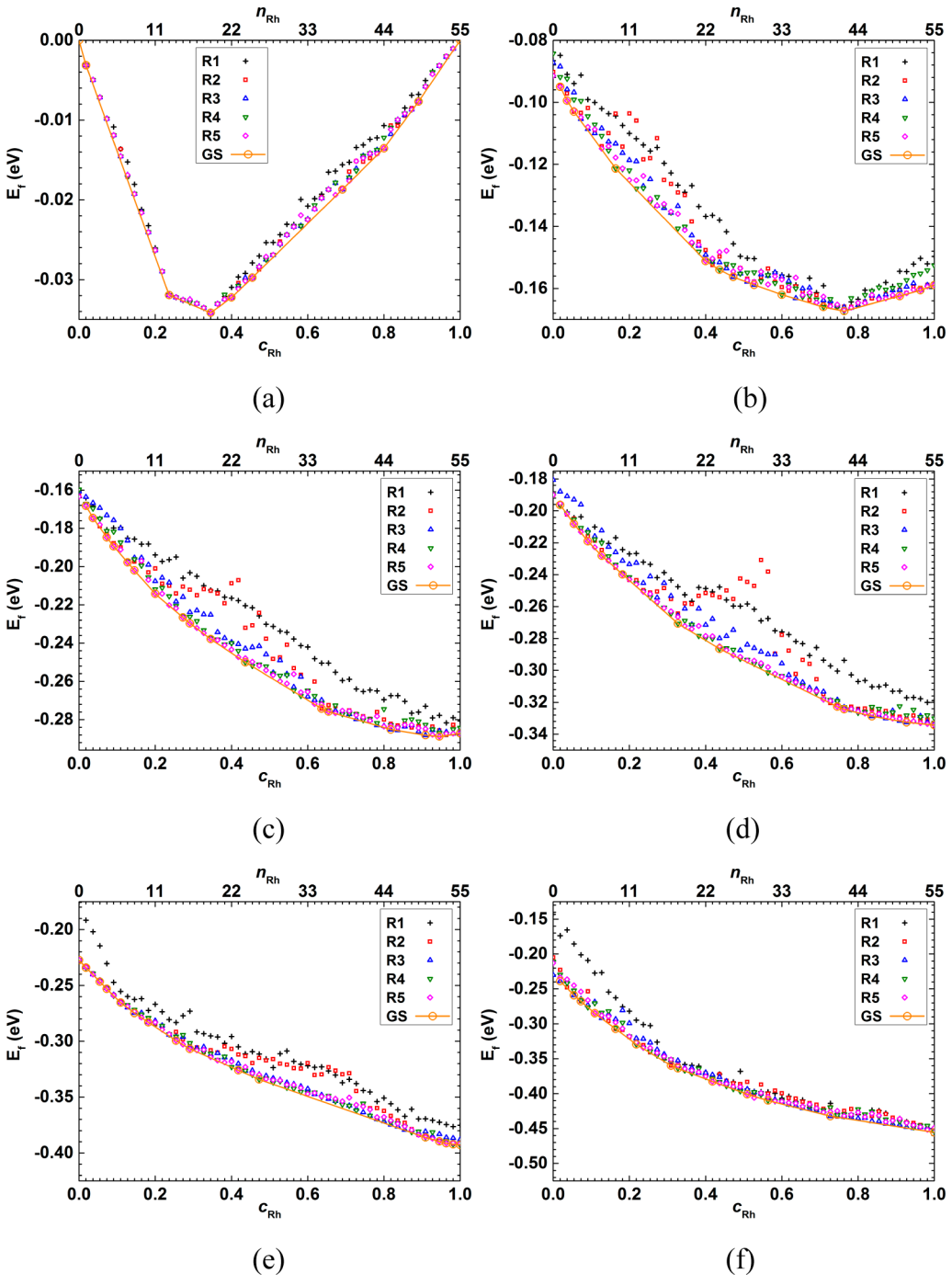

Figure 2. Ground-state hulls with DFT-evaluated E_f as a function of Rh composition, c_{Rh}. R1 to R5 refers to predicted GS configurations from each of the five rounds of CE plus thermal annealing. The O-coverages are (a) 0, (b) 10, (c) 20, (d) 24, (e) 30, and (f) 40. Selected GS configurations are shown in Figure 3.

adsorbates, computational details for DFT calculations with Vienna Ab initio Simulation Package (VASP)[48,49] and MC simulations are provided in the Supporting Information.

Results and Discussion. *Nanoalloy Stability and Groundstates.* For Pd–Rh–O NPs, after five rounds of CE fitting using a thermal-annealing GS search with DFT verification, no new GSs are found. The CV-1 score is 0.77 and 1.42 meV for the metal–metal and all ECIs, respectively. Figure 2 shows the GS hull versus n_{Rh} at selected O-coverages (n_O = 0, 10, 20, 30 and 40) for CE fitting, and one O-coverage (n_O = 24) for validation. Representative GS configurations are presented in Figure 3 to show the site preferences. The other validating O-coverage (n_O = 12) is shown in Supporting Information Figure.S1. The improvement can also be seen in the decreasing mean absolute error (MAE) in predicting new structural energies in Supporting Information Figure.S2. The improvement from the first three rounds is significant, but five rounds are needed for proper details to reach a MAE below 2 meV.

At zero O-coverage (n_O = 0), as seen in Figures 2a and 3a, PdRh NP has a simple alloying behavior and strong Rh-core/Pd-shell preference. With increasing n_{Rh}, Rh first occupies the

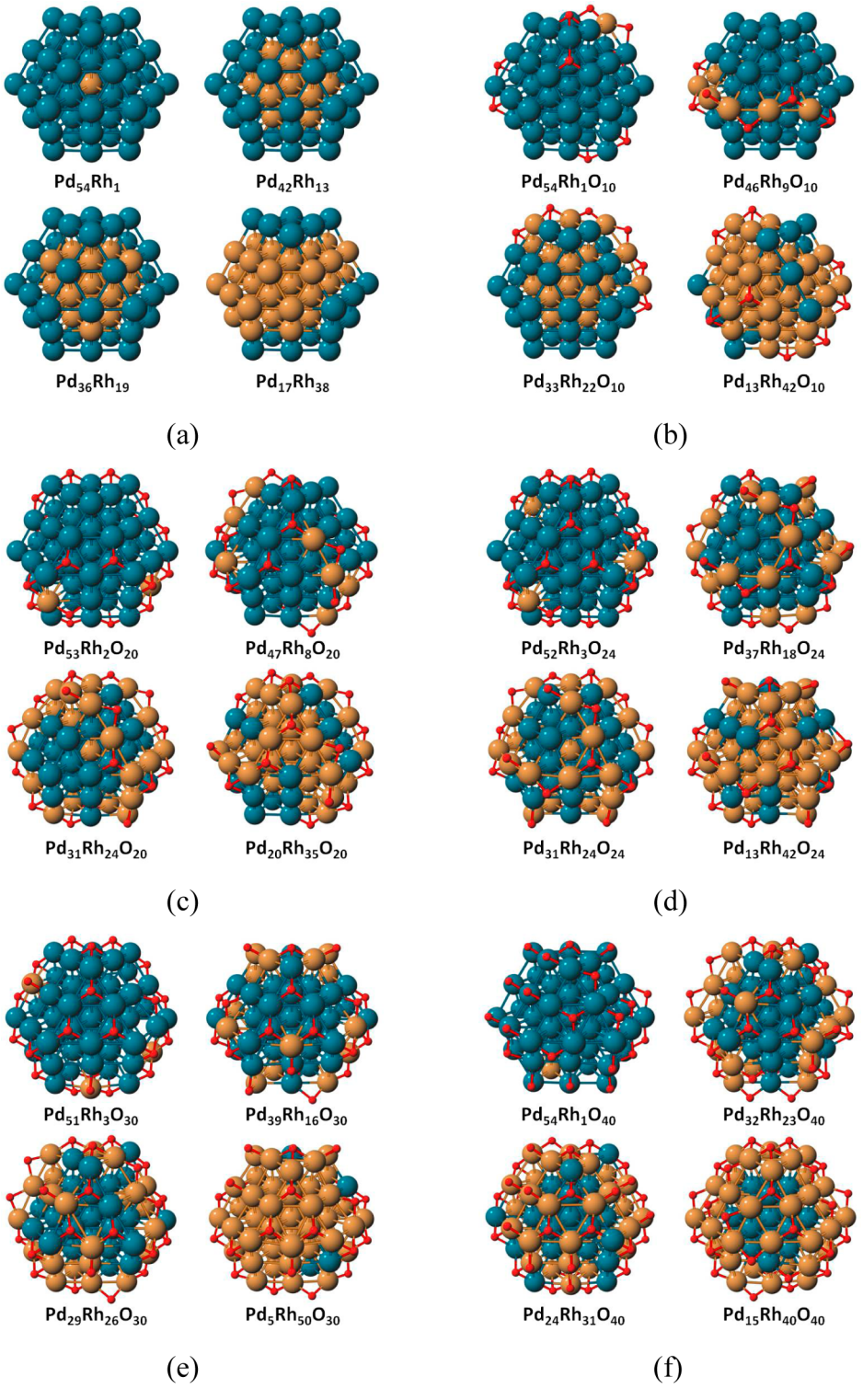

Figure 3. Selected configurations on the GS hull (Figure 2) at different O-coverages: (a) 0, (b) 10, (c) 20, (d) 24, (e) 30, and (f) 40. Blue, brown, and red spheres indicate Pd, Rh, and O, respectively.

central-core site followed by the second-core sites to form the perfect core−shell NP, and then the {100}-center site in the shell, denoted by the GSs at n_{Rh} = 13 and 19.

At n_O = 10 (Figures 2b and 3b), a single Rh atom prefers the corner site in the shell (as opposed to the central-core site at n_O = 0) and binds to two O at the brf sites; the other O also bind to the corner Pd atom in pairs but with each sitting on hcp site across the corner Pd. As n_{Rh} increases, more Rh stays in the shell to bind with O; in $Pd_{46}Rh_9O_{10}$, each Rh binds to two O, forming a "half-ring" around the NP. For n_{Rh} > 9, Rh starts to occupy the core sites; in $Pd_{33}Rh_{22}O_{10}$, core sites are fully occupied by Rh, while the Rh−O ring in the shell persists. Upon further increase in composition, extra Rh occupies the shell again and the Rh−O ring breaks up to accommodate more Rh. For the Rh-rich $Pd_{13}Rh_{42}O_{10}$, the favorable O adsorption site to Rh is also the hcp site, where a pair of O binds on the

dx.doi.org/10.1021/nl503519m | Nano Lett. 2014, 14, 7077−7084

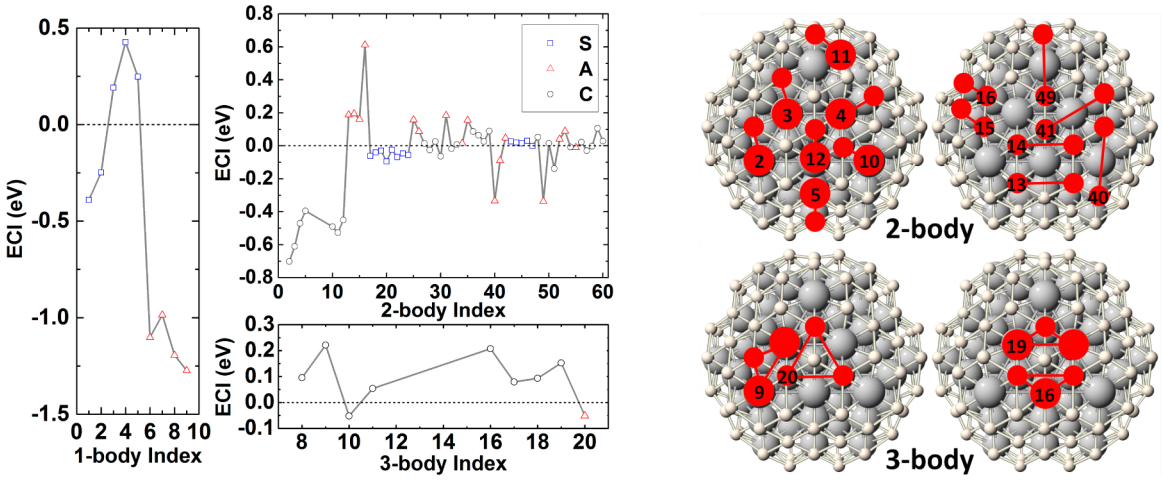

Figure 4. Optimized ECIs of (a) 1-, 2-, and 3-body with selected ones shown in (b). No data are shown for the indices of the excluded ECIs due to very short distances. ECIs among substrate (S), adsorbate (A), and the coupled (C) are indicated in blue squares, red triangles, and black circles, respectively. Indices for 1-body ECIs are illustrated in Figure 1.

{111} facets across the corner Rh. Comparing to the most stable $Pd_{36}Rh_{19}$ for bare NP at −0.032 eV/atom, E_f starts at −0.090 eV/atom for $Pd_{55}O_{10}$, and reaches −0.162 eV/atom for $Pd_{13}Rh_{42}O_{10}$ at the bottom of the GS hull.

At n_O = 20 (Figures 2c and 3c), the neighboring hcp sites on the same {111} facet become occupied for the Rh-poor $Pd_{53}Rh_2O_{20}$. A new configuration for Rh−O appears, where Rh at the edge site binds to three O, two hcp sites on the same {111} facet and one brg site on the neighboring {100} facet for maximizing the favorable Rh−O interaction. As n_{Rh} increases, more Rh first stay at the edge and corner sites in the shell as in $Pd_{47}Rh_8O_{20}$, then go into the core as in $Pd_{31}Rh_{24}O_{20}$, until the whole core region is filled with Rh as in $Pd_{20}Rh_{35}O_{20}$.

At n_O = 24, whose DFT energies are not included into the training data set for CE, the convergence of the GSs in Figure 2d is a proof that our optimal ECIs fitted from the selected O-coverages are also good for other O-coverages. The behavior in site occupation is similar to n_O = 20. Compared to $Pd_{31}Rh_{24}O_{20}$ with the same n_{Rh}, $Pd_{31}Rh_{24}O_{24}$ has no second-core site occupied by Rh, demonstrating that an increasing O-coverage tends to reverse the core−shell preference of the bare NP.

At n_O = 30 (Figures 2e and 3e), all 24 hcp on {111} facets and 6 brg sites (one on each {100} facet) are occupied for $Pd_{55}O_{30}$ and $Rh_{55}O_{30}$. For alloyed PdRh NPs with n_{Rh} = 6 or less as in $Pd_{51}Rh_3O_{30}$, this GS configuration of O persists, because Rh solute prefers to bind to two O at hcp sites and one O at brg site. With n_{Rh} > 6, some hcp sites become unoccupied to accommodate more O, because each unoccupied hcp site gives way to the occupation of the adjacent brf and brg sites.

As the O-coverage approaches one monolayer, more hcp sites will be unoccupied in exchange for O binding to brf and brg sites. When the three hcp sites on a {111} facet become empty, the fcc site becomes a favorable O adsorption site. At n_O = 40, for the Rh-poor $Pd_{54}Rh_1O_{40}$, O occupies all the fcc sites and some brf and brg sites, leaving hcp sites empty (see Figure 3f). But in general, the GS at such high O-coverage is a mixture of all four types of adsorption sites. For $Pd_{15}Rh_{40}O_{40}$, all 40 Rh now stay in the shell and the core is purely Pd. Indeed, a total core−shell reversal can be induced by increasing O-coverage.

Effective Cluster Interactions. We plot the ECIs from the optimal CE in Figure 4. Among the nine 1-body ECIs, the first five are for substrate sites. The ECIs for central-core and second-core sites are negative with the central-core being the most favorable for Rh. The 1-body ECIs for the shells sites are all positive with magnitude (energy cost) increasing with the decrease in nearest neighbor (NN) metal coordination. The first pair ECIs among substrate sites are all negative, favoring alike NN atoms. So without O, the PdRh NPs have a strong preference for Rh-core and Pd-shell, explaining the GS in Figure 3a. The other four 1-body ECIs are for the adsorbate sites and are all strongly negative; hcp site is the most favored, followed by brg, fcc, and brf sites. The magnitudes of the 1-body adsorbate ECIs are larger than those for substrate sites, showing that metal−O are much stronger than metal−metal interactions.

Among the 2-body ECIs shown in Figure 4a, the first pair ECIs for the coupled interactions between metal and O are dominant and strongly negative. This means that the Rh−O interactions are stronger than Pd−O. As seen in Figure 4b, the first coupled 2-body ECIs are stronger for brf site (indices 2 and 3), than brg (4 and 5), hcp (10 and 11), and fcc (12) sites. This adds favorability to the brf site for O adsorption with Rh atom when compared to the hcp site, which is the most favored site for 1-body ECI. The positive 2-body ECIs among adsorbates reflect the O−O repulsion (indices 13, 14, 15 and 16), while those negative ones correspond to the ECIs across the metal atom (40, 41, and 49), which explains the appearance of a pair of O binding across metal atom in the GSs. The 3-body coupled ECIs are mostly positive, showing the repulsion and the competition for metal atoms among neighboring O. Lastly, the adsorbate ECI for two NN hcp sites is repulsive while that for three NN hcp sites is weakly attractive. These features of the ECIs explain well the GS configurations in Figure 2 and 3.

Monte Carlo Simulations Compared to Experiment. Using the optimal ECIs, we can evaluate structural energies accurately for a huge number of configurations needed in MC simulations to study the configurational thermodynamics of O-covered PdRh NPs. Specifically, we study the observed reversal of core−

dx.doi.org/10.1021/nl503519m | *Nano Lett.* 2014, 14, 7077−7084

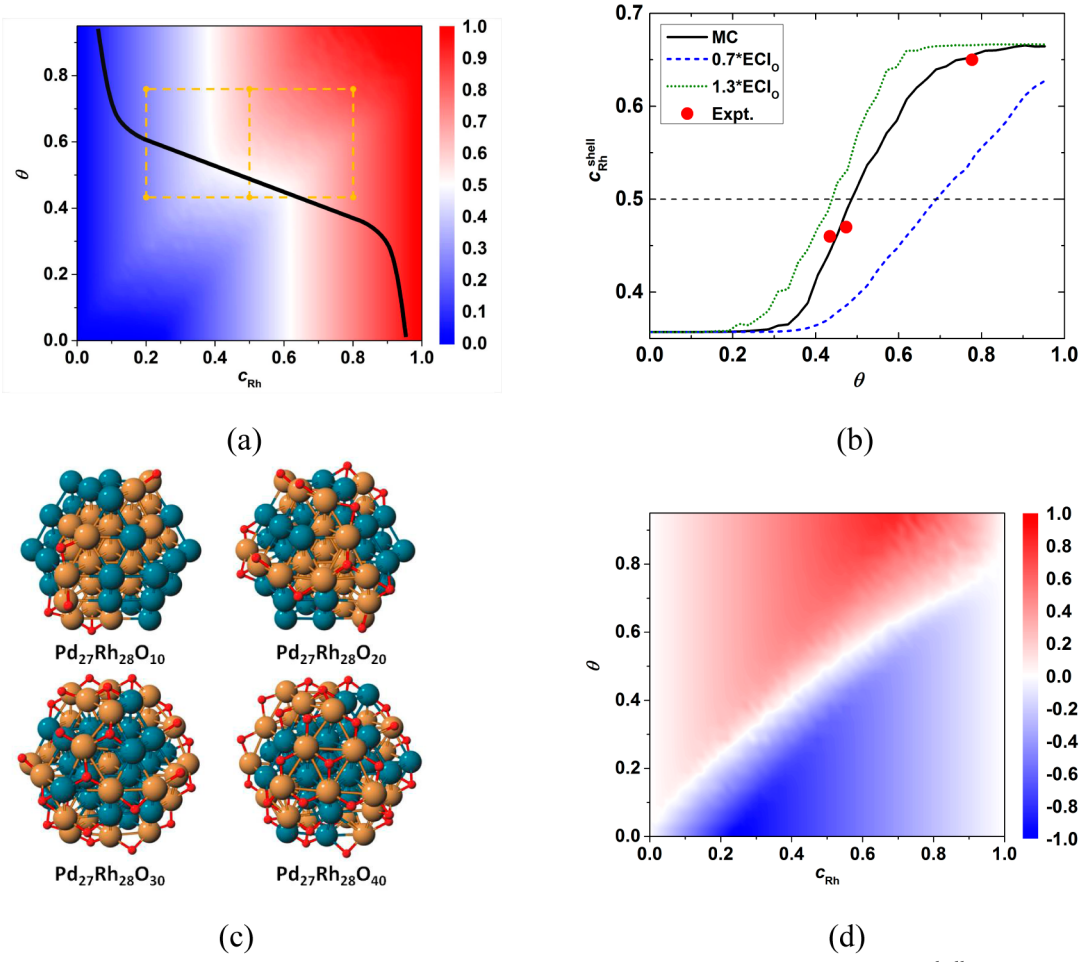

Figure 5. (a) From MC simulations at 583 K, the shell concentration of Rh, c_{Rh}^{shell}, across overall Rh composition, c_{Rh}, and O-coverage, θ. Horizontal dashed lines are the effective θ (from 0.43 to 0.78) extracted from experimental data (ref 8), and the vertical dashed lines are the c_{Rh} used in the experiment (0.2, 0.5, and 0.8). Black curve stands for the 50−50 boundary of c_{Rh}^{shell} for a 15 nm NP (see Supporting Information). (b) c_{Rh}^{shell} for $Pd_{27}Rh_{28}$ NP versus θ compared to experimental data (ref 8), (c) lowest-energy configurations for $Pd_{27}Rh_{28}$ NP with selected O-coverage, and (d) Rh concentration difference between shell and core, $c_{Rh}^{shell}-c_{Rh}^{core}$. Dashed (dotted) line in (b) is from simulations when the optimal O-related ECIs are changed by a factor of 0.7 (1.3).

shell preference induced by O-coverage in PdRh NPs. Qualitatively, it is easy to understand the reversal is due to the stronger Rh−O than Pd−O interactions. As O-coverage increases, more Rh will move to shell and, beyond a certain O-coverage, Rh becomes the majority species in the shell. However, to design an alloyed NP catalyst under working conditions, our MC simulations with DFT-derived ECIs provide quantitative predictions.

At 583 K, we plot in Figure 5a the Rh shell concentration, c_{Rh}^{shell}, as functions of the overall c_{Rh} and O-coverage, θ. Clearly, the coverage-composition map is divided by the 50−50 boundary into two regions. In the Pd-rich (Rh-rich) region on the left (right), the shell is always Pd-rich (Rh-rich), regardless of the O-coverage. The core−shell reversal only happens in the range of c_{Rh} = 0.4−0.6, or around $Pd_{0.5}Rh_{0.5}$. Given the opposite strong core−shell preferences with and without O-coverage for PdRh NPs, the size of this transition zone across c_{Rh} is due to a NP geometric size effect (see Supporting Information). For the large PdRh NPs with a diameter of 15 ± 2 nm in the in situ AP-XPS experiments,[8,9] the boundary is at c_{Rh} = 0.05 (0.95) for high (low) O-coverage. The black curve in Figure 5a is drawn as the boundary for the 15 nm NP by keeping the same slope in the core−shell reversal transition zone, because this slope is determined by the relative strength of metal−O to metal−metal interactions and temperature (see Supporting Information).

In experiments,[8,9] the 15 nm NPs are in a gas pressure of 0.1 Torr for different chemical conditions, where the surface metal oxides start to form. The AP-XPS probes 0.7 nm deep into the surface. Tao et al. have also reported the percentage of metal oxides in the shell region of the $Pd_{0.5}Rh_{0.5}$ NP in reducing and oxidizing conditions, along with metal concentration.[8] Without taking the detailed structure of the surface metal oxides, we extract the ratio of O versus metal as the renormalized effective O-coverage. Our MC simulations give the shell enrichment of Rh induced by the changes in such effective O-coverage, not for the absolute gas pressure. The range of the effective O-coverage from 0.43 to 0.78 and the three NP compositions at c_{Rh} = 0.2, 0.5, and 0.8 in experiment are shown as dashed lines in Figure 5a.

On the Rh-rich side, at c_{Rh} = 0.8 the 15 nm NP does not experience core−shell reversal as observed, unless going to lower O-coverages or more reducing conditions. On the Pd-rich side, at c_{Rh} = 0.2 the 15 nm NP should have the core−shell reversal according to this analysis, but it was not observed. Note that the effective O-coverage range is derived from the

experimental data on the NPs at c_{Rh} = 0.5. For the Pd-rich (Rh-rich) side with the same gas pressure, the coverage will be lower (higher) due to the weaker Pd−O bonds than Rh−O. This will move the range away from the 50−50 boundary.

For the core−shell reversal at c_{Rh} = 0.5, our MC-predicted c_{Rh}^{shell} of the $Pd_{27}Rh_{28}$ NP versus θ agrees very well with the experimental data, see Figure 5b. Four GS atomic configurations with selected O-coverages from low to high (n_O = 10, 20, 30, and 40) are shown in Figure 5c. The experimental data in the oxidizing condition is with O_2. The data in the reducing condition is with NO + CO, where CO reduces the dissociated NO to form CO_2 and N_2. So, the surface coverage of N is small and we can compare to our MC simulation. For the other oxidizing condition with NO instead of O_2, there is a considerable coverage of N. Because the adsorbed N can change the metal core−shell compositional profile due to the different metal−N and metal−O bond strengths, we cannot compare that to our present results which do not include N. The agreement in Figure 5b at multiple instances is not coincidental: the transition zone depends critically on the relative strength in metal−metal, metal−O, and O−O interactions. If we change the magnitudes of the ECIs that involve O to be 30% less (more), it will change the position where the core−shell reversal happens; see the dashed (dotted) lines in Figure 5b.

To account for the NP size effect on the metal−O and metal−metal interactions, we estimate the strength of such interactions with the single-site configuration-weighted segregation energy and the O-adsorption energy difference, which are the thermodynamic driving forces for the opposite core−shell preference, for different NP sizes (see Supporting Information). Because the thermodynamic driving forces both increase with decreasing NP size, the ratio between them actually has a much less variation (last column in Supporting Information Table S1). This explains why the simulated Rh shell concentrations from our small NP at the same effective O-coverage range can reproduce the experimental data on the large NPs.

Figure 5d shows the core−shell preference for Rh defined as, $c_{Rh}^{shell}-c_{Rh}^{core}$, reflecting Rh preference for the shell over core as a function of c_{Rh} and O-coverage. For a fixed c_{Rh} at low O-coverage, negative $c_{Rh}^{shell}-c_{Rh}^{core}$ means the majority of Rh prefer to stay in the NP core due to the larger surface energy and smaller atomic size than Pd. With increasing O-coverage, stronger Rh−O bonding (over Pd−O) draws Rh from the core to the shell, switching the sign of $c_{Rh}^{shell}-c_{Rh}^{core}$. For a fixed O-coverage, at small c_{Rh}, positive $c_{Rh}^{shell}-c_{Rh}^{core}$ means Rh tends to segregate to the NP shell to form stronger Rh−O bonds. But as c_{Rh} increases and available O are all consumed, the extra Rh will go into the core region. Then, to make the shell a more favorable place for Rh than the core a higher O-coverage is needed but the relationship is not quite linear.

Conclusions. We have extended the CE formalism of nonexchangeable coupled lattices to treat alloyed NPs with adsorbates to study heterogeneous nanocatalysts in operational conditions, including core−shell reversal induced by adsorbates. For the CE in the heterogeneous system, we also develop a new, two-step strategy to obtain effective cluster interactions that account for the relative strength of interactions and yield small prediction errors and fast convergence. The DFT-derived interactions fitted at the selected adsorbate-coverages across the metal composition are shown to be good at all coverages and compositions. Using these interactions with Monte Carlo simulated annealing, we have studied the configurational thermodynamics of a 55-atom cuboctahedral PdRh NP versus Rh composition and up to a monolayer O-coverage. We find that core−shell NPs only around 50% Rh experience a core−shell reversal induced by O-coverage due to the geometric size effect. The simulated shell concentrations of Rh in the small $Pd_{0.5}Rh_{0.5}$ NP across the same effective O-coverage range agree with the experimental data on large NPs, reflecting the same origin for core−shell reversal, that is, the relative strength of metal−O, metal−metal, and O−O interactions. The new computational capability reveals detailed site occupations as functions of nanoalloy composition and adsorbate-coverage, providing direct design information for nanoalloy catalysts under operating conditions.

■ ASSOCIATED CONTENT

Ⓢ Supporting Information

Cluster expansion fitting for heterogeneous nanoparticle-adsorbate system, DFT computational details, and additional results for the effects of temperature and size on core−shell behavior. This material is available free of charge via the Internet at http://pubs.acs.org.

■ AUTHOR INFORMATION

Corresponding Authors

*E-mail: llw@ameslab.gov.
*E-mail: ddj@ameslab.gov.

Notes

The authors declare no competing financial interest.

■ ACKNOWLEDGMENTS

Work at Ames Laboratory was supported by the U.S. Department of Energy (DOE), Office of Basic Energy Sciences, Division of Materials Science and Engineering (method), with partial support (L.L.W. for catalysis application) from the Division of Chemical Science, Geosciences, and Bioscience (DEFG02-03ER15476), and L.D.R.D. funding for materials discovery and design at Ames Laboratory. The research was performed at the Ames Laboratory, which is operated for DOE by Iowa State University under Contract No. DE-AC02-07CH11358. We modified the initial thesis version of T.T.K. code developed by T.L.T. at the University of Illinois Urbana−Champaign (http://hdl.handle.net/2142/24227), which was supported by the National Science Foundation (grant DMR-012448) and the Materials Computation Center (Grant DMR-0325939).

■ REFERENCES

(1) Hansen, P. L.; Wagner, J. B.; Helveg, S.; Rostrup-Nielsen, J. R.; Clausen, B. S.; Topsoe, H. *Science* **2002**, *295*, 2053−2055.
(2) Nolte, P.; Stierle, A.; Jin-Phillipp, N. Y.; Kasper, N.; Schulli, T. U.; Dosch, H. *Science* **2008**, *321*, 1654−1658.
(3) Nolte, P.; Stierle, A.; Kasper, N.; Jin-Phillipp, N. Y.; Jeutter, N.; Dosch, H. *Nano Lett.* **2011**, *11*, 4697−4700.
(4) Lim, B.; Jiang, M. J.; Camargo, P. H. C.; Cho, E. C.; Tao, J.; Lu, X. M.; Zhu, Y. M.; Xia, Y. N. *Science* **2009**, *324*, 1302−1305.
(5) Wang, L.-L.; Johnson, D. D. *J. Am. Chem. Soc.* **2007**, *129*, 3658−3664.
(6) Li, L.; Wang, L. L.; Johnson, D. D.; Zhang, Z. F.; Sanchez, S. I.; Kang, J. H.; Nuzzo, R. G.; Wang, Q.; Frenkel, A. I.; Li, J.; Ciston, J.; Stach, E. A.; Yang, J. C. *J. Am. Chem. Soc.* **2013**, *135*, 13062−13072.
(7) Yoshida, H.; Kuwauchi, Y.; Jinschek, J. R.; Sun, K. J.; Tanaka, S.; Kohyama, M.; Shimada, S.; Haruta, M.; Takeda, S. *Science* **2012**, *335*, 317−319.

(8) Tao, F.; Grass, M. E.; Zhang, Y.; Butcher, D. R.; Renzas, J. R.; Liu, Z.; Chung, J. Y.; Mun, B. S.; Salmeron, M.; Somorjai, G. A. *Science* **2008**, *322*, 932−934.
(9) Tao, F.; Grass, M. E.; Zhang, Y.; Butcher, D. R.; Aksoy, F.; Aloni, S.; Altoe, V.; Alayoglu, S.; Renzas, J. R.; Tsung, C.-K.; Zhu, Z.; Liu, Z.; Salmeron, M.; Somorjai, G. A. *J. Am. Chem. Soc.* **2010**, *132*, 8697−8703.
(10) Renzas, J. R.; Huang, W. Y.; Zhang, Y. W.; Grass, M. E.; Hoang, D. T.; Alayoglu, S.; Butcher, D. R.; Tao, F.; Liu, Z.; Somorjai, G. A. *Phys. Chem. Chem. Phys.* **2011**, *13*, 2556−2562.
(11) Xin, H. L. L.; Alayoglu, S.; Tao, R. Z.; Genc, A.; Wang, C. M.; Kovarik, L.; Stach, E. A.; Wang, L. W.; Salmeron, M.; Somorjai, G. A.; Zheng, H. M. *Nano Lett.* **2014**, *14*, 3203−3207.
(12) Besenbacher, F.; Chorkendorff, I.; Clausen, B. S.; Hammer, B.; Molenbroek, A. M.; Nørskov, J. K.; Stensgaard, I. *Science* **1998**, *279*, 1913−1915.
(13) Kyriakou, G.; Boucher, M. B.; Jewell, A. D.; Lewis, E. A.; Lawton, T. J.; Baber, A. E.; Tierney, H. L.; Flytzani-Stephanopoulos, M.; Sykes, E. C. H. *Science* **2012**, *335*, 1209−1212.
(14) Maroun, F.; Ozanam, F.; Magnussen, O. M.; Behm, R. J. *Science* **2001**, *293*, 1811−1814.
(15) Shan, S. Y.; Petkov, V.; Yang, L. F.; Luo, J.; Joseph, P.; Mayzel, D.; Prasai, B.; Wang, L. Y.; Engelhard, M.; Zhong, C. J. *J. Am. Chem. Soc.* **2014**, *136*, 7140−7151.
(16) Metropolis, N.; Rosenbluth, A. W.; Rosenbluth, M. N.; Teller, A. H.; Teller, E. *J. Chem. Phys.* **1953**, *21*, 1087−1092.
(17) Hohenberg, P.; Kohn, W. *Phys. Rev.* **1964**, *136*, B864−B871.
(18) Kohn, W.; Sham, L. J. *Phys. Rev.* **1965**, *140*, A1133−A1138.
(19) Sanchez, J. M.; Ducastelle, F.; Gratias, D. *Physica A* **1984**, *128*, 334−350.
(20) Tepesch, P. D.; Garbulsky, G. D.; Ceder, G. *Phys. Rev. Lett.* **1995**, *74*, 2272−2275.
(21) Muller, P.; Hejral, U.; Rutt, U.; Stierle, A. *Phys. Chem. Chem. Phys.* **2014**, *16*, 13866−13874.
(22) Mittendorfer, F.; Seriani, N.; Dubay, O.; Kresse, G. *Phys. Rev. B* **2007**, *76*, 233413.
(23) Schlatter, J. C.; Taylor, K. C. *J. Catal.* **1977**, *49*, 42−50.
(24) Gandhi, H. S.; Graham, G. W.; McCabe, R. W. *J. Catal.* **2003**, *216*, 433−442.
(25) Renzas, J. R.; Huang, W. Y.; Zhang, Y. W.; Grass, M. E.; Somorjai, G. A. *Catal. Lett.* **2011**, *141*, 235−241.
(26) Wang, S. B.; Zhu, W.; Ke, J.; Lin, M.; Zhang, Y. W. *ACS Catal.* **2014**, *4*, 2298−2306.
(27) Moss, R. L.; Gibbens, H. R. *J. Catal.* **1972**, *24*, 48−56.
(28) Sanchez, J. M.; Stark, J. P.; Moruzzi, V. L. *Phys. Rev. B* **1991**, *44*, 5411−5418.
(29) Asta, M.; Wolverton, C.; de Fontaine, D.; Dreyssé, H. *Phys. Rev. B* **1991**, *44*, 4907−4913.
(30) Wolverton, C.; Asta, M.; Dreyssé, H.; de Fontaine, D. *Phys. Rev. B* **1991**, *44*, 4914−4924.
(31) Sluiter, M. H. F.; Watanabe, Y.; Fontaine, D. d.; Kawazoe, Y. *Phys. Rev. B* **1996**, *53*, 6137−6151.
(32) van de Walle, A.; Ceder, G. *J. Phase Equilib.* **2002**, *23*, 348−359.
(33) Zarkevich, N. A.; Johnson, D. D. *Phys. Rev. Lett.* **2004**, *92*, 255702.
(34) Blum, V.; Hart, G. L. W.; Walorski, M. J.; Zunger, A. *Phys. Rev. B* **2005**, *72*, 165113.
(35) Hart, G. L. W.; Blum, V.; Walorski, M. J.; Zunger, A. *Nat. Mater.* **2005**, *4*, 391−394.
(36) Zarkevich, N. A.; Tan, T. L.; Johnson, D. D. *Phys. Rev. B* **2007**, *75*, 104203.
(37) Zarkevich, N. A.; Tan, T. L.; Wang, L. L.; Johnson, D. D. *Phys. Rev. B* **2008**, *77*, 144208.
(38) Chepulskii, R. V.; Butler, W. H.; van de Walle, A.; Curtarolo, S. *Scr. Mater.* **2010**, *62*, 179−182.
(39) Wang, L.-L.; Tan, T. L.; Johnson, D. D. *Phys. Rev. B* **2012**, *86*, 035438.
(40) Tan, T. L.; Wang, L.-L.; Johnson, D. D.; Bai, K. *Nano Lett.* **2012**, *12*, 4875−4880.
(41) Yuge, K. *J. Phys.: Condens. Matter* **2010**, *22*, 245401.
(42) Yuge, K. *Phys. Rev. B* **2011**, *84*, 085451.
(43) Mueller, T. *Phys. Rev. B* **2012**, *86*, 144201.
(44) Wang, L.-L.; Johnson, D. D. *J. Am. Chem. Soc.* **2009**, *131*, 14023−14029.
(45) Connolly, J. W. D.; Williams, A. R. *Phys. Rev. B* **1983**, *27*, 5169−5172.
(46) Han, B. C.; Van der Ven, A.; Ceder, G.; Hwang, B.-J. *Phys. Rev. B* **2005**, *72*, 205409.
(47) Kerscher, T. C.; Landgraf, W.; Podloucky, R.; Muller, S. *Phys. Rev. B* **2012**, *86*, 195420.
(48) Kresse, G.; Furthmuller, J. *Phys. Rev. B* **1996**, *54*, 11169−11186.
(49) Kresse, G.; Furthmuller, J. *Comput. Mater. Sci.* **1996**, *6*, 15−50.